Liver-innervating vagal sensory neurons play an indispensable role in the development of hepatic steatosis in mice fed a high-fat diet.

Jiyeon Hwang[1,2], Woo-Hyun Cho[1,2], Streamson C. Chua Jr.[1,2], Gary J. Schwartz[1,2], and Young-Hwan Jo[1,2,3*]

Affiliations

[1]The Fleischer Institute for Diabetes and Metabolism
[2]Division of Endocrinology, Department of Medicine
[3]Department of Molecular Pharmacology, Albert Einstein College of Medicine, NY, USA

*** Corresponding author: young-hwan.jo@einsteinmed.edu**
Departments of Medicine and Molecular Pharmacology
Albert Einstein College of Medicine,
1300 Morris Park Ave, Bronx, NY 10461
Tel: 718-430-3495

Abstract

The visceral organ-brain axis, mediated by vagal sensory neurons in the vagal nerve ganglion, is essential for maintaining various physiological functions. These vagal sensory neurons relay interoceptive signals from visceral organs to the medulla. In this study, we investigate the influence of the loss of the liver-brain axis on energy balance, glucose homeostasis, and hepatic steatosis in mice under obesogenic conditions. A subset of vagal sensory neurons innervating the liver is located in both the left and right ganglia, projecting centrally to the nucleus of the tractus solitarius, area postrema, and dorsal motor nucleus of the vagus, and peripherally to the periportal areas in the liver. Ablation of the liver-brain axis via caspase-induced selective destruction of advillin-positive neurons prevents diet-induced obesity in male and female mice, and these outcomes are associated with increased energy expenditure. Although males and females exhibit improved glucose homeostasis following disruption of the liver-brain axis, only male mice display increased insulin sensitivity. Furthermore, loss of the liver-brain axis limits the progression of hepatic steatosis in male and female mice fed a steatogenic diet. Therefore, modulation of the liver-brain axis may present a therapeutic strategy for restoring lipid metabolism and glucose homeostasis in obesity and diabetes.

Introduction

Communication between the visceral organs and the brain is required to maintain metabolic homeostasis. Vagal sensory neurons present in the vagus nerve ganglia transmit interoceptive signals from visceral organs to the medulla via the vagus nerve(1). Vagal sensory neurons are highly heterogeneous in their molecular identities, anatomical connections, and physiological roles(1-3). Each type of vagal sensory neurons with unique molecular features has a specific target organ such as the larynx, stomach, intestine, pancreas, heart, and lung(3-10). Despite the important contribution of the liver to energy metabolism, glucose homeostasis, energy storage, immunity, and detoxification(11), surprisingly, there is little information about the vagal sensory neurons innervating the liver.

The liver comprises several different cell populations, such as parenchymal cells, hepatocytes, and non-parenchymal cells, including Kupffer cells, cholangiocytes, stellate cells, and sinusoidal endothelial cells(11, 12). It has been described that only a limited number of vagal sensory neurons in the left nodose ganglion project to the liver in rats(13). The peripheral nerve terminals of the vagal sensory neurons innervating the liver are primarily present in the bile ducts and portal veins, whereas no afferent terminals are observed in the hepatic parenchyma of rats(14). Although the central projection sites of vagal sensory neurons innervating the liver remain unknown, the central axon terminals of vagal sensory neurons are generally localized to the nucleus of the tractus solitarius (NTS), area postrema (AP), and dorsal motor nucleus of the vagus (DMV)(15). Intriguingly, the vagal sensory neurons innervating the wall of the portal vein in rats project predominantly to the DMV, suggesting the presence of a monosynaptic vago-vagal reflex linking primary vagal afferent terminals arising from the liver to vagal motor neuron somata(16).

Neurophysiological studies have shown that the activity of the hepatic vagal afferent nerves and neurons is modulated by changes in glucose and amino acid levels in rodents(17, 18), suggesting that vagal sensory neurons innervating the liver may detect circulating nutrients. The vagal sensory neurons innervating the liver have been demonstrated to regulate aspects of lipolysis and thermogenesis in both white and brown adipose tissues by sensing and transmitting information regarding excess energy balance to the brain(19). In this study, we sought to identify the molecular identity of vagal sensory neurons innervating the liver and their role in controlling overall energy balance. We found that a small subset of vagal sensory neurons in the left and

right nodose ganglia projected to the liver and that the loss of the liver-brain axis prevented diet-induced obesity (DIO) and hepatic steatosis in both female and male mice fed a high-fat diet (HFD).

Results

Molecular identification of vagal sensory neurons innervating the liver

We first sought to determine whether the vagal sensory neurons in the vagus nerve ganglia innervate the liver. We expressed the Cre recombinase in the vagus nerve ganglia by administering retrograde adeno-associated viruses (AAVrg) encoding the Cre recombinase gene (AAVrg-Cre) to the liver of Rosa26-floxed-STOP-Cas9-eGFP (Rosa26-eGFP^{f}) mice (Fig. 1a). This knock-in strain showed strong GFP expression in both the cell bodies and nerve terminals of the infected cells, following Cre expression in our previous study(20). GFP immunostaining revealed the presence of GFP-positive cells in the nodose ganglion (Fig. 1b). Contrary to previous studies showing that vagal sensory neurons innervating the liver are primarily located in the left nodose ganglion in rats[1](13, 21), the number of GFP-positive neurons was similar in both vagus nerve ganglia (Fig. 1c), implying that each ganglion contained a similar number of liver-innervating vagal sensory neurons.

We then examined the central projection sites of the vagal sensory neurons innervating the liver in the medulla. We used brainstem tissues from the same Rosa26-eGFP^{f} mice that were administered AAVrg-Cre into the liver. Following the tissue-clearing process, we conducted a 3D imaging analysis of the tissues, which revealed a high density of GFP-positive nerve terminals in the intermediate part of the NTS and, to a lesser extent, in the commissural part of the NTS and the area postrema (AP) (Fig. S1a). Additionally, scattered GFP-positive axon terminals were observed in the dorsal motor nucleus of the vagus (DMV). (Fig. S1a and Movie S1). Intriguingly, those projecting to the DMV were primarily found on the left side (Fig. S1a).

We then sought to determine the molecular identity of vagal sensory neurons innervating the liver by performing single-nucleus RNA sequencing (snRNA-Seq) of vagal sensory neurons in Rosa26-eGFP^{f} mice administered AAVrg-Cre into the liver (Fig. 1d). We were able to identify approximately 9,000 cells from 30 nodose ganglia collected from 8 males and 7 females. Among them, approximately 6,000 cells had neuronal marker genes such as microtubule associated protein 2 (*Map2*), synapsin 1 and 2 (*Syn1* and *Syn2*), and solute carrier family 17 member 6

(*Slc17a6*). However, we found only 7 genetically tagged vagal sensory neurons (Table S1) because of the technical limitations associated with a limited number of liver-innervating vagal sensory neurons. We grouped the seven vagal sensory neurons innervating the liver and compared them with other vagal sensory neurons. As shown in Fig. 1e, they expressed neuronal marker genes such as synapsin 1 (*Syn1*), voltage-gated sodium channel α subunit 10 (*Scn10a*), voltage-gated potassium channel subfamily C member 2 (*Kcnc2*), and the sensory neuron-specific actin-binding protein advillin (*Avil)*(22). These liver-innervating vagal sensory neurons expressed several ion channel subtypes including chemosensitive transient receptor potential cation channel subfamily V member 1 (*Trpv1*), temperature-sensitive TRP subfamily M member 3 (*Trpm3*) and subfamily A member 1 (*Trpa1*), and mechanosensitive piezo-type ion channel component 2 (*Piezo2*) (Fig. 1f), indicating that they are polymodal sensory neurons. These neurons also expressed the opioid receptor μ-1 (*Oprm1*), the neuropeptide Y receptor type 2 (*Npy2R*), the cholecystokinin A receptor (*Cckar*), and the cannabinoid receptor type 1 (*Cnr1*). Intriguingly, vagal sensory neurons innervating the liver highly expressed genes involved in lipid metabolism such as ATP citrate lyase (*Acyl*), fatty acid synthetase (*Fasn*), and stearoyl-CoA desaturase 2 (*Scd2*), compared to other vagal sensory neurons (Fig. 1g). We also noted that liver-innervating sensory neurons expressed genes related to cell adhesion, neuronal migration, axonal growth, and survival. These genes included uncoordinated-5 receptor C and D (*Unc5C and D*), neuregulin 1 and 3 (*Nrg1 and 3*), transmembrane protein with EGF-like and two follistatin-like domains (*Tmeff2*), kirre like nephrin family adhesion molecule 3 (*Kirrel3*), and others (Fig. 1h and i). Hence, our initial molecular study suggests that vagal sensory neurons innervating the liver are polymodal and are molecularly distinct from other vagal sensory neurons.

The liver is innervated by a subset of Avil-positive vagal sensory neurons

Based on our snRNA-Seq results and a previous study indicating that chemosensitive vagal sensory neurons express *Avil* gene(2), we used the Avil^{CreERT2} strain to identify vagal sensory neurons that innervate the liver. Additionally, we employed AAVrg-FLEX-jGCamp7s, which expresses Cre-inducible jGCamp7s, due to the observation that GFP expression with this vector was more robust compared to other AAV vectors encoding eGFP and tdTomato. Administering AAVrg-FLEX-jGCamp7s to the medial and left lobes of the livers of Avil^{CreERT2} mice resulted in the selective labeling of vagal sensory neurons innervating the liver in the

nodose ganglia (Fig. 2a-c). As shown in Figure 2, both nodose ganglia exhibited a small number of GFP-positive cells. Approximately 10% of Avil-positive vagal sensory neurons were positive for GFP.

We investigated the peripheral nerve terminals of the vagal sensory neurons innervating the liver. For these experiments, we crossbred the Avil^{CreERT2} strain with floxed-Stop channelrhodopsin (ChR2)-tdTomato mice (Avil$^{CreERT2:ChR2\text{-}tdTomato}$), as the ChR2-tdTomato fusion protein displayed strong expression in nerve terminals. To label the nerve terminals of those innervating the liver, we administered AAVrg-FLEX-GFP into the livers of Avil$^{CreERT2:ChR2\text{-}tdTomato}$ mice (Fig. 3a). Immunostaining revealed numerous tdTomato-positive nerve fibers in the periportal area (Fig. 3b). These fibers were positive for GFP, indicating that they were the nerve fibers originated in Avil-positive vagal sensory neurons.

We further examined the peripheral nerve terminals of the vagal sensory neurons innervating the liver. To label nerve terminals of liver-innervating vagal sensory neurons, AAVrg-FLEX-jGCamp7s or AAVrg-FLEX-GFP viruses were injected into the livers of Avil^{CreERT2} mice (Fig. 3c and Fig. S2a). Co-staining with an antibody against the presynaptic marker synapsin 1 (Syn1) revealed that GFP-positive nerve terminals were also positive for Syn1, indicating that these are nerve terminals (Fig. 3d and e). We also found that Avil-positive nerve terminals were co-labeled with an anti-GFP antibody in the periportal area (Fig. S2b), whereas there were no Avil-positive nerves in the pericentral zone (Fig. S2c). Next, we administered anterograde AAV1-FLEX-GFPsm-Myc directly into the left nodose ganglion of Avil^{CreERT2} mice (Fig. 3f). Under these experimental conditions, we also found the GFP-and Myc-positive nerve terminals primarily around the periportal, but not pericentral, areas (Fig. 3g). Taken together, both our anterograde and retrograde tracing results strongly support the fact that the liver receives synaptic input from Avil-positive vagal sensory neurons.

Loss of the liver-brain axis causes weight loss and increases energy expenditure.

The hepatic portal vein carries nutrients and hormones from the gastrointestinal tract(23). As vagal sensory neurons sent projections to the periportal regions of the liver and expressed lipid-sensing TRP receptors, it is possible that vagal sensory neurons innervating the liver may detect changes in nutrients and transmit this information to the brain. We thus investigated the impact of the loss of the liver-brain axis on energy balance under obesogenic conditions. To

ablate the liver-brain axis, we expressed genetically engineered taCaspase-3 (taCasp3)(24) in the vagal sensory neurons innervating the liver by injecting AAVrg-FLEX-taCasp3-TEVp into the livers of Avil^{CreERT2} mice (Fig. 4a). To determine whether the retrograde expression of taCasp3-TEVp ablates liver-projecting vagal sensory neurons, we administered the retrograde tracer Fluoro-Gold into livers of Avil^{CreERT2} mice injected with AAVrg-FLEX-taCasp3-TEVp and examined the number of Fluoro-Gold-positive vagal sensory neurons. We found that there was a significant reduction of liver-projecting vagal sensory neurons (Fig. S3a, b, and c). Moreover, unlike the Avil^{CreERT2} mice injected with AAVrg-FLEX-jGCamp7s, we did not observe any GFP-positive nerve terminals in the periportal areas (Fig. S4a, b, and c), which provides further evidence of the loss of liver-projecting vagal sensory innervation of the liver.

Under these experimental conditions, measurements of body weight showed a significant difference in body weight between the groups, starting from 4 weeks of HFD feeding. The experimental male mice gained significantly less weight than control mice (Fig. 4b). This was accompanied by a significant decrease in both fat mass and fat-free mass in the experimental mice compared with the controls (Fig. 4c and d). We then examined whether changes in food intake and/or energy expenditure in male mice fed HFD result in decreased body weight. Measurement of daily food intake revealed that both groups consumed similar amounts of food during the light and dark phases (Fig. 4e). We thus investigated if there was a difference in the energy expenditure between the groups by placing animals in metabolic cages. The experimental mice consumed more O_2 and produced more CO_2 than the control mice during the light and dark phases (Fig. 4f and g), resulting in a significant increase in total energy expenditure (TEE) over a 24-hour period (Fig. 4h). The respiratory energy ratio (RER) and locomotor activity did not differ between the groups (Fig. 4i, j, and k). Analysis of covariance (ANCOVA) using body weight as a covariate showed no differences in the slopes (Fig. 4l), suggesting that body fat did not have a substantial impact on TEE.

We then investigated whether females lacking the liver-brain axis respond similarly to HFD feeding. Ablating the liver-brain axis caused a significant reduction in body weight in female mice as well (Fig. 5a). In contrast to male mice, this reduction was primarily associated with decreased fat mass but not fat-free mass (Fig. 5b and c). Female mice lacking hepatic vagal sensory neurons displayed no difference in food intake compared to controls (Fig. 5d). Indirect calorimetry analysis revealed that VO_2, VCO_2, and TEE in experimental mice were significantly

higher than those in control mice (Fig. 5e, f, and g). Namely, increased energy expenditure seems to be the main factor in preventing DIO in female mice as well. There were no differences in the RER and locomotor activity between the two groups (Fig. 5h, i, and j). Intriguingly, ANCOVA analysis revealed that body weight significantly influenced TEE (Fig. 5k), implying that fat tissue may significantly impact energy expenditure in females.

Loss of the liver-brain axis improves glucose tolerance and insulin sensitivity in mice fed HFD

We next examined the impact of the loss of the liver-brain axis on systemic glucose homeostasis during HFD feeding. Measuring the baseline (non-fasting) and fasting glucose levels following 10 weeks of HFD feeding revealed that both non-fasting and fasting blood glucose levels were significantly lower in the experimental male mice than in the control male mice (Fig. 6a and b). Intraperitoneal glucose tolerance tests (i.p.GTT) to determine if there were any changes in the ability to dispose of a glucose load showed that the blood glucose levels of the experimental mice in response to a bolus of glucose (i.p., 2 g/kg) were significantly lower than those of the control mice (Fig. 6c and d). We evaluated the glucose concentration over time in male mice following i.p. insulin injection. Significantly lower blood glucose levels were observed in the experimental group than in the control group during the insulin tolerance tests (ITT) (Fig. 6e). Improved insulin tolerance in the experimental group was associated with decreased basal and fasting insulin levels relative to those in the control group (Fig. 6f and g).

Likewise, female mice lacking hepatic vagal sensory neurons exhibited lower basal and fasting blood glucose levels than the control females (Fig. 7a and b). Female mice in the experimental group displayed improved glucose tolerance during the GTT compared to the control group (Fig 7c and d). However, there was no noticeable difference in insulin sensitivity between the two groups during the ITT (Fig. 7e). The basal insulin levels were significantly lower in the experimental group compared to the control group, while the fasting insulin levels were similar (Fig. 7f and g).

Loss of the liver-brain axis prevents hepatic steatosis in HFD-fed mice.

We investigated whether the loss of the liver-brain axis affects hepatic lipid metabolism. To assess the degree of hepatic steatosis, we conducted a thorough examination, including

assessment of the overall appearance and weight of the liver, and employed histological analysis in conjunction with Oil Red O staining. The livers of the control group turned yellowish when they were fed HFD for 10 weeks, while the livers of the experimental mice were red (Fig. 8a). The liver weight was significantly lower in the experimental mice than in the control mice (Fig. 8b). Hematoxylin and Eosin (H&E) staining revealed clear differences between the experimental and control male mice (Fig. 8c). In other words, control mice displayed numerous large and small lipid droplets and ballooned hepatocytes, primarily in the pericentral regions, compared to experimental mice. Oil Red O staining further confirmed hepatic fat accumulation in control mice (Fig. 8d).

Given the lack of lipid droplets in the livers of experimental male mice, we measured hepatic triglyceride (TG) levels. The experimental mice displayed a substantial decrease in hepatic TG levels compared with the control mice (Fig. 8e). Reverse transcription-quantitative polymerase chain reaction (RT-qPCR) analysis of liver tissues from the experimental mice revealed a significant decrease in the expression of the lipogenic transcription factor sterol regulatory element-binding protein 1-c (*Srebp-1c*), in comparison to the controls (Fig. 8f). This was accompanied by downregulation of its target genes, including acetyl-coenzyme A carboxylase 1 (*Acaca*), fatty acid synthase (*Fasn*), and stearoyl-CoA desaturase-1 (*Scd1*) (Fig. 8f). In addition, the impairment of the liver-brain axis downregulated the fatty acid translocase *Cd36* and the fatty acid transmembrane transporters *Fatp3* and *Fatp4* gene expression (Fig. 8g). These results indicate that the loss of the liver-brain axis may lead to a reduction in *de novo* lipogenesis (DNL) and fatty acid uptake, thereby preventing the onset of hepatic steatosis in male mice fed HFD.

In female mice, there was no difference in liver color (Fig. 9a). The liver weight was slightly but significantly reduced in the experimental group compared to the control group (Fig. 9b). H & E and Oil red O staining revealed that the control group exhibited small lipid droplets in the liver parenchyma, whereas the experimental group displayed fewer such droplets (Fig. 9c and d). Consistent with these findings, the experimental mice demonstrated a decrease in hepatic TG compared to the control mice (Fig. 9e). In contrast to the experimental male mice, the experimental female mice showed no significant difference in the expression of the lipogenic genes (Fig. 9f). Nonetheless, female mice lacking liver-innervating vagal sensory neurons exhibited decreased *Cd36* and *Fatp3* expression levels (Fig. 9g), which was consistent with the

findings in male mice. The findings imply that liver-innervating vagal sensory neurons are crucial for the development of hepatic steatosis in mice when they are fed a high-fat diet.

Discussion

This study provides molecular, anatomical, and functional evidence for the pivotal role of the liver-brain axis in controlling energy balance, glucose homeostasis, and hepatic steatosis in mice fed HFD. First, vagal sensory neurons innervating the liver exhibited distinct molecular characteristics compared to other types of vagal sensory neurons. Second, both vagus nerve ganglia were found to contain vagal sensory neurons that innervate the liver. Third, these sensory neurons sent peripheral nerve projections primarily to the periportal area of the liver, and their central axonal terminals were localized to the NTS and AP, and to a lesser extent, in the DMV. Fourth, loss of the liver-brain axis prevented the development of DIO in both males and females largely due to increased energy expenditure. Fifth, male and female mice without vagal sensory innervation of the liver displayed lower blood glucose levels and improved systemic glucose tolerance. Notably, male but not female mice lacking vagal sensory neurons innervating the liver showed improved insulin resistance. Lastly, the loss of the liver-brain axis prevented HFD-induced hepatic steatosis in male and female mice. However, the extent of hepatic lipid accumulation and the underlying cellular mechanisms appeared to differ between male and female mice.

The vagus nerve ganglion contains vagal sensory neurons that innervate diverse visceral organs, including the larynx, stomach, intestine, pancreas, heart, and lung(3-10). The highly specialized cellular, molecular, and anatomical organization of vagal sensory neurons has been shown to be crucial for the proper detection and integration of interoceptive signals to control metabolic homeostasis and other vital functions, such as breathing and reward(1-10). As each organ has different tissue layers and physiological functions, vagal sensory neurons innervating different internal organs appear to have their own molecular identities and anatomical connections(1-10). In other words, distinct types of vagal sensory neurons possess specialized nerve terminals based on their modalities and functions(3, 5, 8, 10). Single-cell RNA-seq analysis has revealed 12-37 molecularly distinct subtypes of vagal sensory neurons(2, 5, 25). Importantly, the molecular identity of vagal sensory neurons appears to play a major role in determining their functional properties(3, 5-8, 10). For example, vagal sensory neurons that control the digestive system include vasoactive intestinal peptide-, glucagon-like peptide 1 receptor-, oxytocin receptor-, and G protein-coupled receptor 65-expressing neurons(5, 8). Interestingly, distinct types of vagal sensory neurons (somatostatin- vs. CGRP-positive cells)

innervate different parts of the stomach(5). Those innervating the lungs are purinergic receptor P2RY1-positive neurons and neuropeptide Y receptor Y2-expressing neurons(6). Pancreatic islets are innervated by vagal sensory neurons expressing substance P, calcitonin gene-related peptide (CGRP), and 5-HT3 receptors(7).

Despite significant advances in the characterization of vagal sensory neurons that project to the visceral organs, the molecular identity of those innervating the liver remains unknown. Our single-nucleus RNA-seq analysis identified seven neurons out of ~ 6,000 neurons from 15 mice largely due to the fact that a very limited number of vagal sensory neurons innervate the liver. However, our results revealed that liver-projecting vagal sensory neurons were polymodal C-fiber sensory neurons described in the study by the Ernfors research group (i.e., NG12 to NG18(2)). In fact, polymodal C-fiber vagal sensory neurons expressed *Scn10a*, *Trpv1, Trpa1*, *Npy2r*, and *Cckar*(2) which were also expressed in liver-projecting vagal sensory neurons. Liver-innervating vagal sensory neurons were found mainly in the periportal area surrounding the hepatic arteries, bile ducts, and portal veins and expressed mechano-sensing Piezo channels(26), lipid-sensing TRPA1, TRPM3, and TRPV1 channels(27), and gut-derived hormone CCK receptors. This multimodality of liver-innervating vagal sensory neurons would be particularly important because hepatic homeostasis highly relies on adequate perfusion and microcirculation via the dual hepatic arterial and portal venous blood supply, as well as the fenestrated sinusoids. These anatomical and molecular features would enable them to accurately measure blood pressure, assess the levels of various nutrients and peptides, and relay this information to the brain for processing and interpretation.

Intriguingly, our study revealed a significant expression of genes associated with lipid metabolism in liver-projecting vagal sensory neurons, such as *Acly*, *Fasn*, and *Scd2*. It has been shown that fatty acid metabolism in the brain, particularly the hypothalamus, exerts a significant influence on the regulation of food intake and energy metabolism(28-30), suggesting that fatty acid metabolism and its associated metabolites in hypothalamic neurons may serve as indicators of nutrient status. Similarly, the increased lipogenic machinery in liver-innervating vagal sensory neurons may imply that they also possess the capability to control energy balance in response to changes in nutrient availability. Additionally, lipogenesis in neurons is critical for several aspects of neuronal function, including dendrite morphogenesis(31), axon growth and regeneration(32). The UNC5 family of netrin receptors (UNC5C and 5D) is involved in axon guidance and

mediates axon repulsion of neuronal growth cones in the developing nervous system(33). Of particular interest is that netrin-1 was found to stimulate the regeneration of the hepatic vagal nerve and the proliferation of hepatocytes in mice following hepatectomy(34). Thus, our initial findings from single-nucleus RNA sequencing provides significant information regarding their potential implications for a range of physiological processes.

Retrograde labeling with horseradish peroxidase showed that a very small number of vagal sensory neurons in the left nodose projected to the liver in rats(13). In contrast to this early finding, we found that the left and right nodose ganglia possessed similar numbers of liver-innervating vagal sensory neurons. A prior neuronal tracing study showed that vagal sensory neurons projecting to the hepatic portal vein were also located in the left and right nodose ganglia of rats(16). Furthermore, gut-innervating vagal sensory neurons were detected in both nodose ganglia as well(9). It should be noted that the vagal sensory neurons innervating the liver traverse the common hepatic branch of the vagus nerve, which also includes those projecting to the portal vein and the gastroduodenal tract(15). These prior studies support our results that liver-projecting vagal sensory neurons are located in the left and right nodose ganglia.

Interestingly, the vagal sensory neurons in the left and right ganglia appear to have different physiological functions(9). Optogenetic stimulation of vagal sensory neurons in the left nodose ganglion reduced food intake, whereas stimulation of the right nodose ganglion were implicated in brain reward pathways(9). These distinct and independent functions of vagal sensory neurons in the left versus right nodose ganglion are likely due to their different central projection sites in the medulla(9). The left nodose ganglion had a different pattern of projections than the right one. The left nodose ganglion projected to the posterior part of the AP and lightly to the NTS, in contrast to the right nodose ganglion, which sent projections to the ventromedial NTS and to a lesser extent to the posterior part of the AP(9). In line with these findings, we found that the central axonal projection sites of those innervating the liver were unevenly distributed in the medulla. The intermediate part of the NTS received dense axonal projections and scattered nerve terminals were observed in the commissural part of the NTS and the AP. Interestingly, the DMV on the left side of the medulla was innervated by liver-projecting vagal sensory neurons. Since the vagal sensory neurons project to the ipsilateral part of the medulla, the vagal sensory neurons in the right nodose ganglion may transmit to higher brain centers,

whereas the vagal sensory neurons in the left nodose ganglion would play a role in the vago-vagal reflex pathways.

The peripheral nerve terminals of vagal sensory neurons innervating the liver were observed primarily in the bile ducts and portal veins, whereas no afferent terminals were observed in the hepatic parenchyma of rats(14). In our preparations, the periportal region had dense innervation of vagal sensory neurons innervating the liver. As the portal vein delivers nutrients and hormones from the gut, liver-projecting vagal sensory neurons may detect changes in nutrients and transmit this information to the NTS. The projection sites of the NTS include the parabrachial nucleus (PBN), ventrolateral medulla, hypothalamus, and bed nucleus of the stria terminalis(35-40). Both local interneurons and projection neurons in the NTS were implicated in the control of various body functions. For instance, local GABAergic interneurons influenced the activity of liver-projecting parasympathetic cholinergic neurons in the DMV, thereby regulating the hepatic glucose output(41). Norepinephrine-expressing projection neurons in the NTS controlled feeding behavior(39, 40, 42). Interestingly, activation of the NE-expressing neurons in the NTS (NTS^{NE}) to CGRP-expressing neurons in the PBN pathway reduced(40), whereas stimulation of the NTS^{NE} to agouti-related peptide (Agrp)-containing neurons in the arcuate nucleus of the hypothalamus (ARC^{Agrp}) pathway promoted, feeding(39). Importantly, the $NTS^{NE} \rightarrow ARC^{Agrp}$ pathway appeared to be involved in the control of glucoprivic feeding(39). In addition, NE-positive neurons sent projections to parasympathetic cholinergic neurons in the DMV as well(42). In our preparations, the impairment of the liver-brain axis induced the anti-obesity effect. This would be due to the fact that the brain receives the inadequate information on excess energy balance via vagal sensory neurons innervating the liver. In other words, the brain would not monitor changes in the body energy state. Consequently, this sensory impairment would cause an increase in energy expenditure instead of storing excess nutrients in the liver, as observed in our study.

In summary, the liver-brain axis contributes to the regulation of energy balance, systemic glucose tolerance, insulin sensitivity, and hepatic steatosis, depending on the nutrient status in healthy and obesogenic conditions. An implantable vagus nerve stimulator has been approved by the Food and Drug Administration (FDA) to treat epilepsy and depression. Modulating the liver-brain axis via the vagus nerve may offer a promising therapeutic approach for improving lipid metabolism and glucose homeostasis in obesity and diabetes.

Methods

Animals

All mouse care and experimental procedures were approved by the Institutional Animal Care Research Advisory Committee of Albert Einstein College of Medicine.

Eight-nine-week-old Avil^{CreERT2} (stock # 032027) and Rosa26-floxed-STOP-Cas9-eGFP mice (stock# 024857) were purchased from the Jackson Laboratory. Mice were housed in cages at a controlled temperature (22 °C) with a 12:12 h light-dark cycle and fed a high-fat diet (HFD; Research Diets, D12492; 20% calories by carbohydrate, 20% by protein, and 60% by fat) for 10-12 weeks, with water provided *ad libitum*. The mice were administered intraperitoneal injections of 75 mg tamoxifen/kg body weight on five consecutive days. The tamoxifen solution was prepared by dissolving it in a mixture of 90% corn oil and 10% ethanol.

Viral injection

We used AAVrg-Cre (Addgene 55636-AAVrg, titer; 2.2 x10^{13} pfu/ml), AAVrg-FLEX-GFP (Addgene 51502-AAVrg, titer; 2.3 x10^{13} pfu/ml), AAVrg-FLEX-jGCamp7s (Addgene 104491, titer; 2.5 x10^{13} pfu/ml). Avil^{CreERT2} mice received a total volume of 20 ul of viral injection into the medial and left lobes of the livers. Mice were killed 5 and 10 weeks post-viral inoculation.

To ablate liver-innervating vagal sensory neurons, a total volume of 10-20 ul of AAVrg-FLEX-taCasp3-TEVp (titer >1 × 10^{12} pfu/ml; Addgene 45580) was injected into the medial and left lobes of the livers of Avil^{CreERT2} mice. AAVrg-FLEX-GFP (Addgene 51502-AAVrg, titer > 1 × 10^{13} pfu/ml) was used as control.

Clear, unobstructed brain imaging cocktails (CUBIC) tissue clearing and immunostaining.

The CUBIC method(43) was used to clear brainstem tissues. Mice were perfused with 4% (w/v) paraformaldehyde (PFA) in PBS. Brain tissues were collected and post-fixed in 4% PFA at 4C° for 24 h. The tissue samples were sectioned using a vibratome at a thickness of 300 um. The sections were immersed in CUBIC reagent 1 (25 wt% urea, 25 wt% quadrol, and 15 wt% Triton X-100) with gentle shaking at 37C° for 3 days. After decolorization, the sections were washed three times with PBS at RT for 2 h and then incubated in a blocking solution composed of 1% donkey serum, 0.5% BSA, 0.3% Triton X-100, and 0.05% sodium azide for 3 h at room temperature (RT). Tissue samples were incubated with a rabbit anti-GFP (Rockland, 600-401-215, 1:200) for 5 days at RT with mild shaking and washed three times with PBS (each for at least 2 h). Following wash-out, the tissue samples were incubated with an Alexa Fluor 488

donkey anti-rabbit IgG (1:200, Invitrogen, A21206) for 3 days at RT. The tissues were washed and immersed in CUBIC-reagent 2 (50 wt% sucrose, 25 wt% Urea, 10wt% Triethanolamine, and 0.1%(v/v) Triton X-100) for 1 d and mounted with a mixture of mineral oil and silicone oil. Z-stack images were obtained using a Leica SP8 confocal microscope, and 3D construction was performed using the AIVIA community (version 12.1) and Leica application suite X.

Immunostaining

Mice were anesthetized with isoflurane (3%) and transcardially perfused with 4% paraformaldehyde. Nodose ganglia, liver, and brain were post-fixed in 4% paraformaldehyde overnight in a cold room and then in 30% sucrose the following day. Tissues were sectioned using a cryostat at 16-20 μm. The sections were incubated with 0.3% Triton X-100 at room temperature (RT) for 30min, and then blocked in PBS buffer containing 5% donkey serum, 2% bovine serum albumin and 0.15% Triton X-100 for 1hr at RT and then incubated with goat anti-GFP (Novus, NB100-1770, 1:500), rabbit anti-advillin (Abcam, Ab72210, 1:1000), mouse anti-c-Myc (Invitrogen, 13-2500, 1:1,000) antibodies for overnight at RT, and then sections were washed three times in PBS and incubated with AlexaFluor 594 donkey anti-rabbit IgG (Jackson immunoresearch, 711-585-152, 1:500), AlexaFluor 488 donkey anti-goat IgG (Invitrogen, A11055, 1:500), and AlexaFluor 568 donkey anti-mouse IgG (Invitrogen, A10037, 1:500) for 1hr at RT. The sections were washed, dried, and mounted using VECTASHIELD medium containing DAPI. Images were acquired using a Leica SP8 confocal microscope.

For histological analysis, the liver tissues were embedded in paraffin and cut into 5 μm thickness. The sections were stained with hematoxylin and eosin. Lipid droplet accumulation was visualized by Oil Red O staining of the frozen liver sections. H&E and Oil Red O slides of liver sections were scanned using a fast scanner. Representative tissue areas were captured using Slideviewer software (version 2.6).

Measurement of body weight, body composition, and blood glucose

Body weight was measured weekly at 9 a.m. Body composition for fat mass and fat-free mass was assessed using the EchoMRI system. Blood samples were collected from the mouse tail, and a small drop of blood was placed on the test strip of a glucose meter.

Assessment of glucose tolerance and insulin tolerance

For the GTT, the experimental and control mice were fasted for 15 h (6:00 pm–9:00 am) 10 weeks post-viral inoculation. Sterile glucose solution was administered intraperitoneally at a

concentration of 2 g/kg (glucose/body weight) at time zero. Blood glucose levels were measured at 15, 30, 60, 90, and 120 min after glucose injection. Blood glucose levels were plotted against time after glucose injection, and the area under the curve (AUC) was calculated and compared between experimental and control groups. For the ITT, the mice were fasted for 4 h (9:00 am to 1:00 pm). Blood glucose levels were measured at 0, 15, 30, 60, 90, and 120 min after i.p. injection of insulin (1 U/kg). We immediately injected glucose (2 g/kg) if the mice appeared ill due to insulin-induced hypoglycemia.

Assessment of energy expenditure

Mice were individually housed in calorimeter cages (Oxymax, Columbus Instruments) and acclimated to the respiratory chambers for two days prior to gas exchange measurements. Indirect calorimetry was performed for three days at the end of 10 weeks. O_2 consumption and CO_2 production were measured for each mouse at 10-min intervals over a 24-h period. The respiratory exchange ratio was calculated as the ratio of CO_2 production to the O_2 consumption. Since there was no difference in food intake, VO_2 was normalized to the lean body mass. Locomotor activity in the X-Y and Z planes was measured using infrared beam breaks in calorimetry cages.

RT-qPCR

Liver tissues were collected from the experimental and control groups–10-12 weeks post viral inoculation. Liver tissues were homogenized in TRIzol reagent (ThermoFisher Scientific, 15596-018), and total RNAs were isolated according to the manufacturer's instructions. First-strand cDNAs were synthesized using the SuperScript III First-Strand synthesis kit (ThermoFisher Scientific, 18080-051). qPCR was performed in sealed 96-well plates with SYBR Green I master Mix (Applied Biosystems, A25742) using a Quant Studio 3 system (Applied Biosystems). qPCR reactions were prepared in a final volume of 20 ul containing 2 ul cDNAs, and 10 ul of SYBR Green master mix in the presence of primers at 0.5 uM. Beta-actin (*Actb*) was used as an internal control for quantification of each sample. Amplification was performed under the following conditions: denaturation at 95°C for 30 s, followed by 40 cycles of denaturation at 95°C for 30 s and annealing/extension at 60°C for 1 min.

We examined the following genes: *Srebp1c* (NM_001358315.1), *Chrebp* (NM_021455.5), *Acly* (NM_134037.3), *Acaca* (NM_133360.3), *Fasn* (NM_007988.3), *Scd1* (NM_009127.4), *Cd36* (NM_007643.5), *Fatp1* (NM_011977.3), *Fatp2* (NM_011978.2), *Fatp3*

(NM_011988.3) *and Fatp4* (NM_011989.4). All the primer sequences were validated with "Primer BLAST" primer design program to ensure specificity for the target gene. Melt curves and gel electrophoresis were analyzed to confirm the specificity of the PCR products. Relative gene expression was determined using a comparative method ($2^{-\Delta\Delta CT}$).

Single-nucleus RNA sequencing

Nuclei isolation and single-nucleus RNA sequencing were performed by Singulomics Corporation (Singulomics.com, Bronx, NY). Thirty nodose ganglia were collected from 8 male and 7 female Rosa26-eGFP^f injected with AAVrg-Cre into the liver 4 weeks after viral injection. Immediately after tissue collection, 16 nodose ganglia from males and 14 nodose ganglia from females were flash-frozen. Tissue was then homogenized and lysed with Triton X-100 in RNase-free water for nuclei isolation. The isolated nuclei were purified, centrifuged, resuspended in PBS with RNase Inhibitor, and diluted to 700 nuclei/µl for standardized 10x capture and library preparation protocol using 10x Genomics Chromium Next GEM 3' Single Cell Reagent kits v3.1 (10x Genomics, Pleasanton, CA). The libraries were sequenced with Illumina NovaSeq 6000 (Illumina, San Diego, CA).

The libraries were sequenced with ~200 million PE150 reads per sample on Illumina NovaSeq. The raw sequencing reads were analyzed with mouse reference genome (mm10) with the addition of human growth hormone poly(A) (hgGH-poly(A)) transgene sequence that was found in AAVrg-Cre using Cell Ranger v7.1.0. Introns were included in the analysis. To further clean the data, we applied Debris Identification using Expectation Maximization (DIEM) program[44] to filter the barcodes (from raw_feature_bc_matrix of each sample), keeping barcodes with debris scores < 0.5, number of features (genes) > 250, and UMI count > 1000.

Following the default aggregate analysis by cellranger aggr, we employed the cellranger reanalyze function, focusing exclusively on the clean barcodes. The UMAP projection was generated separately and then loaded to the Loupe Browser for downstream analysis. The UMAP projection was produced through Harmony integration, which involved using a Seurat object that incorporated normalized data with selected variable features and principal components(45). Initially, each sample underwent sctransform v2 normalization to identify integration features via Seurat. After merging the normalized objects, integration features were manually picked, and 20 principal components were computed. Harmony integration aimed to unify data from different samples to improve downstream analysis quality. The Harmony algorithm then facilitated the

creation of a UMAP visualization, set with 'harmony' reduction and dimensions 1 to 20. Louvain clustering followed, applying 'harmony' reduction within the FindNeighbors function and the FindClusters function at a 0.5 resolution, all within the Seurat framework. The differential expression was conducted using the 10x Genomics Loupe Browser (version 7).

Measurement of hepatic TG and plasma insulin levels

Liver samples were harvested from mice with or without liver-innervating sensory neurons. Tissue samples were weighed and homogenized in 1 mL of a diluted NP-40 solution to solubilize triglycerides. The samples were centrifuged at 16,000 × g to remove the insoluble material. The TG levels were measured using a TG assay kit (Cayman Chemical, 10010303).

Blood samples from the experimental and control groups were collected from the retroorbital plexus using heparinized capillary tubes. Whole blood was centrifuged at 12,000 × g for 10 min, and plasma was separated and stored at -20°C until use. Plasma insulin concentrations were determined using two-site sandwich ELISA kits (Mercodia, 10-1247-0).

Statistics

All statistical results are presented as the mean ± SEM. Statistical analyses were performed using GraphPad Prism, version 10.0. Two-tailed *t*-tests were used to calculate the p-values for pair-wise comparisons. Time-course comparisons between groups were analyzed using a two-way repeated-measures analysis of variance (RM ANOVA) with Sidak's correction for multiple comparisons. Data were considered significantly different when the probability value was less than 0.05.

Acknowledgments

General: We thank Dr. Shun-Mei Liu and Licheng Wu for their technical assistance.

Funding: This work was supported by the NIH (R01 AT011653 to Y.-H.J, R01 DK092246 to Y.-H.J and G.J.S., P30 DK020541 to Y.-H.J, G.J.S., and S.C.C.Jr).

Author contributions: J.Y.H performed viral injection, immunostaining, Western blotting, ELISA assays, and analyzed data. WHJ injected viral vectors, performed immunohistochemistry, and analyzed data. Y.-H.J designed the study, performed viral injection and immunocytochemistry, analyzed the data, and wrote the manuscript with input from G.J.S. G.J.S. and S.C.C.Jr also designed the study.

Competing interests: The authors declare no conflict of interest.

References cited:

1. Waise TMZ, Dranse HJ, and Lam TKT. The metabolic role of vagal afferent innervation. *Nat Rev Gastroenterol Hepatol.* 2018;15(10):625-36.
2. Kupari J, Haring M, Agirre E, Castelo-Branco G, and Ernfors P. An Atlas of Vagal Sensory Neurons and Their Molecular Specialization. *Cell Rep.* 2019;27(8):2508-23 e4.
3. Zhao Q, Yu CD, Wang R, Xu QJ, Dai Pra R, Zhang L, et al. A multidimensional coding architecture of the vagal interoceptive system. *Nature.* 2022;603(7903):878-84.
4. Bassi JK, Connelly AA, Butler AG, Liu Y, Ghanbari A, Farmer DGS, et al. Analysis of the distribution of vagal afferent projections from different peripheral organs to the nucleus of the solitary tract in rats. *The Journal of comparative neurology.* 2022;530(17):3072-103.
5. Bai L, Mesgarzadeh S, Ramesh KS, Huey EL, Liu Y, Gray LA, et al. Genetic Identification of Vagal Sensory Neurons That Control Feeding. *Cell.* 2019;179(5):1129-43 e23.
6. Chang RB, Strochlic DE, Williams EK, Umans BD, and Liberles SD. Vagal Sensory Neuron Subtypes that Differentially Control Breathing. *Cell.* 2015;161(3):622-33.
7. Makhmutova M, Weitz J, Tamayo A, Pereira E, Boulina M, Almaca J, et al. Pancreatic beta-Cells Communicate With Vagal Sensory Neurons. *Gastroenterology.* 2021;160(3):875-88 e11.
8. Williams EK, Chang RB, Strochlic DE, Umans BD, Lowell BB, and Liberles SD. Sensory Neurons that Detect Stretch and Nutrients in the Digestive System. *Cell.* 2016;166(1):209-21.
9. Han W, Tellez LA, Perkins MH, Perez IO, Qu T, Ferreira J, et al. A Neural Circuit for Gut-Induced Reward. *Cell.* 2018;175(3):665-78 e23.
10. Borgmann D, Ciglieri E, Biglari N, Brandt C, Cremer AL, Backes H, et al. Gut-brain communication by distinct sensory neurons differently controls feeding and glucose metabolism. *Cell metabolism.* 2021;33(7):1466-82 e7.
11. Trefts E, Gannon M, and Wasserman DH. The liver. *Curr Biol.* 2017;27(21):R1147-R51.
12. Baratta JL, Ngo A, Lopez B, Kasabwalla N, Longmuir KJ, and Robertson RT. Cellular organization of normal mouse liver: a histological, quantitative immunocytochemical, and fine structural analysis. *Histochem Cell Biol.* 2009;131(6):713-26.
13. Carobi C, and Magni F. The afferent innervation of the liver: a horseradish peroxidase study in the rat. *Neurosci Lett.* 1981;23(3):269-74.
14. Berthoud HR, Kressel M, and Neuhuber WL. An anterograde tracing study of the vagal innervation of rat liver, portal vein and biliary system. *Anat Embryol (Berl).* 1992;186(5):431-42.
15. Berthoud HR. Anatomy and function of sensory hepatic nerves. *Anat Rec A Discov Mol Cell Evol Biol.* 2004;280(1):827-35.
16. Garcia-Luna C, Sanchez-Watts G, Arnold M, de Lartigue G, DeWalt N, Langhans W, et al. The Medullary Targets of Neurally Conveyed Sensory Information from the Rat Hepatic Portal and Superior Mesenteric Veins. *eNeuro.* 2021;8(1).
17. Niijima A, Torii K, and Uneyama H. Role played by vagal chemical sensors in the hepato-portal region and duodeno-intestinal canal: an electrophysiological study. *Chem Senses.* 2005;30 Suppl 1:i178-9.

18. Grabauskas G, Song I, Zhou S, and Owyang C. Electrophysiological identification of glucose-sensing neurons in rat nodose ganglia. *The Journal of physiology.* 2010;588(Pt 4):617-32.
19. Uno K, Katagiri H, Yamada T, Ishigaki Y, Ogihara T, Imai J, et al. Neuronal pathway from the liver modulates energy expenditure and systemic insulin sensitivity. *Science.* 2006;312(5780):1656-9.
20. Jeong JH, Lee DK, Liu SM, Chua SC, Jr., Schwartz GJ, and Jo YH. Activation of temperature-sensitive TRPV1-like receptors in ARC POMC neurons reduces food intake. *PLoS Biol.* 2018;16(4):e2004399.
21. Teratani T, Mikami Y, Nakamoto N, Suzuki T, Harada Y, Okabayashi K, et al. The liver-brain-gut neural arc maintains the T(reg) cell niche in the gut. *Nature.* 2020;585(7826):591-6.
22. Hasegawa H, Abbott S, Han BX, Qi Y, and Wang F. Analyzing somatosensory axon projections with the sensory neuron-specific Advillin gene. *The Journal of neuroscience : the official journal of the Society for Neuroscience.* 2007;27(52):14404-14.
23. Bacharach SZ, Tordoff MG, and Alhadeff AL. Glucose Sensing in the Hepatic Portal Vein and Its Role in Food Intake and Reward. *Cell Mol Gastroenterol Hepatol.* 2023;16(2):189-99.
24. Yang CF, Chiang MC, Gray DC, Prabhakaran M, Alvarado M, Juntti SA, et al. Sexually dimorphic neurons in the ventromedial hypothalamus govern mating in both sexes and aggression in males. *Cell.* 2013;153(4):896-909.
25. Prescott SL, Umans BD, Williams EK, Brust RD, and Liberles SD. An Airway Protection Program Revealed by Sweeping Genetic Control of Vagal Afferents. *Cell.* 2020;181(3):574-89 e14.
26. Zeng WZ, Marshall KL, Min S, Daou I, Chapleau MW, Abboud FM, et al. PIEZOs mediate neuronal sensing of blood pressure and the baroreceptor reflex. *Science.* 2018;362(6413):464-7.
27. Ciardo MG, and Ferrer-Montiel A. Lipids as central modulators of sensory TRP channels. *Biochim Biophys Acta Biomembr.* 2017;1859(9 Pt B):1615-28.
28. de Moura RF, Nascimento LF, Ignacio-Souza LM, Morari J, Razolli DS, Solon C, et al. Hypothalamic stearoyl-CoA desaturase-2 (SCD2) controls whole-body energy expenditure. *Int J Obes (Lond).* 2016;40(3):471-8.
29. Gao S, Moran TH, Lopaschuk GD, and Butler AA. Hypothalamic malonyl-CoA and the control of food intake. *Physiol Behav.* 2013;122:17-24.
30. Kim EK, Miller I, Aja S, Landree LE, Pinn M, McFadden J, et al. C75, a fatty acid synthase inhibitor, reduces food intake via hypothalamic AMP-activated protein kinase. *The Journal of biological chemistry.* 2004;279(19):19970-6.
31. Ziegler AB, Thiele C, Tenedini F, Richard M, Leyendecker P, Hoermann A, et al. Cell-Autonomous Control of Neuronal Dendrite Expansion via the Fatty Acid Synthesis Regulator SREBP. *Cell Rep.* 2017;21(12):3346-53.
32. Ewan EE, Avraham O, Carlin D, Goncalves TM, Zhao G, and Cavalli V. Ascending dorsal column sensory neurons respond to spinal cord injury and downregulate genes related to lipid metabolism. *Sci Rep.* 2021;11(1):374.
33. Yamagishi S, Bando Y, and Sato K. Involvement of Netrins and Their Receptors in Neuronal Migration in the Cerebral Cortex. *Front Cell Dev Biol.* 2020;8:590009.

34. Wang Z, Jiang T, Aji T, Aimulajiang K, Liu Y, Lv G, et al. Netrin-1 promotes liver regeneration possibly by facilitating vagal nerve repair after partial hepatectomy in mice. *Cell Signal.* 2022;91:110227.
35. Hermann GE, and Rogers RC. Convergence of vagal and gustatory afferent input within the parabrachial nucleus of the rat. *J Auton Nerv Syst.* 1985;13(1):1-17.
36. Kobashi M, and Adachi A. A hepatoportal osmoreceptive afferent projection from nucleus tractus solitarius to caudal ventrolateral medulla. *Brain Res Bull.* 1990;24(6):775-8.
37. Affleck VS, Coote JH, and Pyner S. The projection and synaptic organisation of NTS afferent connections with presympathetic neurons, GABA and nNOS neurons in the paraventricular nucleus of the hypothalamus. *Neuroscience.* 2012;219(1-2):48-61.
38. Shin JW, Geerling JC, and Loewy AD. Inputs to the ventrolateral bed nucleus of the stria terminalis. *The Journal of comparative neurology.* 2008;511(5):628-57.
39. Aklan I, Sayar Atasoy N, Yavuz Y, Ates T, Coban I, Koksalar F, et al. NTS Catecholamine Neurons Mediate Hypoglycemic Hunger via Medial Hypothalamic Feeding Pathways. *Cell metabolism.* 2020;31(2):313-26 e5.
40. Roman CW, Derkach VA, and Palmiter RD. Genetically and functionally defined NTS to PBN brain circuits mediating anorexia. *Nat Commun.* 2016;7:11905.
41. Boychuk CR, Smith KC, Peterson LE, Boychuk JA, Butler CR, Derera ID, et al. A hindbrain inhibitory microcircuit mediates vagally-coordinated glucose regulation. *Sci Rep.* 2019;9(1):2722.
42. Rinaman L. Hindbrain noradrenergic A2 neurons: diverse roles in autonomic, endocrine, cognitive, and behavioral functions. *Am J Physiol Regul Integr Comp Physiol.* 2011;300(2):R222-35.
43. Matsumoto K, Mitani TT, Horiguchi SA, Kaneshiro J, Murakami TC, Mano T, et al. Advanced CUBIC tissue clearing for whole-organ cell profiling. *Nat Protoc.* 2019;14(12):3506-37.
44. Alvarez M, Rahmani E, Jew B, Garske KM, Miao Z, Benhammou JN, et al. Enhancing droplet-based single-nucleus RNA-seq resolution using the semi-supervised machine learning classifier DIEM. *Sci Rep.* 2020;10(1):11019.
45. Hao Y, Hao S, Andersen-Nissen E, Mauck WM, 3rd, Zheng S, Butler A, et al. Integrated analysis of multimodal single-cell data. *Cell.* 2021;184(13):3573-87 e29.

Figure legends

Figure 1. Molecular identification of vagal sensory neurons innervating the liver

a. Schematic illustration of our experimental configurations. AAVrg-Cre viruses were injected into the medial and left lobes of the livers of Rosa26-eGFP^{f} mice.

b. Image from confocal fluorescence microscopy showing GFP-positive cells in the right nodose ganglion of Rosa26-eGFP^{f} mice injected with AAVrg-Cre into the liver. Scale bar, 100 μm

c. Graph showing the number of GFP-positive cells per section in the left and right nodose ganglia.

d. Schematic illustration depicting our experimental process.

e, **f**, **g**, and **h**. Graphs showing enriched genes in liver-projecting vagal sensory neurons (LP VN) compared to other vagal sensory neurons (VN) (neuronal marker genes (e), membrane receptors and ion channels (f), lipogenic genes (g), and genes related to axon growth and maturation (h)).

i. Heatmap plot showing the differential expression of genes between LP VN and VN.

Figure 2. A subset of Avil-positive neurons innervate the liver

a. Schematic illustration of our experimental configurations. AAVrg-FLEX-jGcamp7s viruses were injected into the medial and left lobes of the livers of Avil^{CreERT2} mice.

b and c. Images showing co-expression of GFP and Avil in a subset of neurons in the left and right nodose ganglia of Avil^{CreERT2} mice injected with AAVrg-FLEX-jGcamp7s into the liver. Upper panel: scale bar, 100 μm. Bottom panel: higher magnification view of the yellow square area. Arrowheads represent the vagal sensory neurons that innervate the liver. Scale bar, 10 μm

Figure 3. Vagal sensory neurons send axonal projections to the periportal area.

a and **b**. Schematic illustration of the experimental conditions. AAVrg-FLEX-GFP viruses were injected into the medial and left lobes of the livers of Avil$^{CreERT2;ChR2\text{-}tdTomato}$ mice. Images showing co-expression of GFP and tdTomato at nerve terminals in the periportal area (b). Scale bar, 20 μm

c. Schematic illustration of the experimental configurations. AAVrg-FLEX-jGcamp7s viruses were injected into the medial and left lobes of the livers of Avil^{CreERT2} mice.

d and **e**. Images showing that GFP-positive nerve terminals were also stained with the presynaptic marker Syn1 (red). Left panel: scale bar, 20 μm, right panels: scale bar, 10 μm

f and **g.** Schematic illustration depicting our experimental conditions. Anterograde AAV-FLEX-GFPsm-myc viruses were injected into the left nodose ganglion of of Avil^{CreERT2} mice (f). Most nerve terminals were positive for GFP and Myc, indicating that they were the nerve terminals of Avil-positive vagal sensory neurons innervating the liver. Scale bar, 20 μm. Bottom panel: higher magnification view of the white square area. Arrowheads represent co-expression of Myc and GFP. Bottom panel: scale bar, 20 μm

Figure 4. Loss of the liver-brain axis reduces body weight and increases energy expenditure in male mice fed HFD.

a. Schematic representation of the experimental configurations. AAVrg-FLEX-eGFP and AAVrg-FLEX-taCasp3-TEVp viral vectors were injected directly into the medial and left lobes of the livers of Avil^{CreERT2} mice.

b. Graph showing the changes in body weight of the control (n= 16 mice) and experimental groups (n= 15 mice) during the course of high-fat diet feeding (two-way ANOVA, ***p<0.001)

c and d. Graphs showing the differences in fat mass and fat-free mass between the two groups (control, n= 16 mice; experimental, n=15 mice; unpaired *t*-test, ***p<0.001, *p<0.05).

e. Graphs showing that there was no difference in food intake between the two groups (control, n= 6 mice; experimental mice, n=7 mice).

f and **g.** Summary graphs showing a significant increase in O_2 consumption and CO_2 production in the experimental group compared to the control group (control, n= 6 mice; experimental mice, n=7 mice; unpaired *t*-test, **p<0.01, ***p<0.001).

h. Graph showing that the experimental mice exhibited a significant increase in TEE compared with the control group during the light and dark phases (control, n= 6 mice; experimental mice, n=7 mice; unpaired *t*-test, **p<0.01).

i, j, and k. Graphs showing the RER and locomotor activity in the control and experimental groups (control, n= 6 mice; experimental mice, n=7 mice).

l. ANCOVA analysis showing no difference in the slope between the two groups (control, n= 6 mice; experimental mice, n=7 mice).

Figure 5. Loss of the liver-brain axis reduces body weight and increases energy expenditure in female mice fed HFD.

a. Graph showing the changes in body weight of the control and experimental groups during high-fat diet feeding (control, n= 15 mice; experimental mice, n= 21 mice; Two-way ANOVA, ***p<0.001).

b and c. Graphs show that the experimental mice exhibited lower fat mass than the controls, whereas there was no difference in fat-free mass between the groups (control, n= 15 mice; experimental mice, n= 21 mice; unpaired *t*-test, ***p<0.001).

d. Graphs showing no difference in food intake between the two groups (control, n= 5 mice; experimental mice, n= 8 mice).

e and **f.** Summary graph showing a significant increase in O_2 consumption and CO_2 production in the experimental group compared to the control group (control, n= 6 mice; experimental mice, n= 5 mice; unpaired *t*-test, *p<0.05, **p<0.01).

g. Graph showing that the experimental mice displayed a greater TEE than the control group (control, n= 6 mice; experimental mice, n= 5 mice; unpaired *t*-test, **p<0.01).

h, i and j. Graphs showing no differences in RER or locomotor activity between the experimental and control groups (control, n= 6 mice; experimental mice, n= 5 mice).

k. ANCOVA analysis showing a significant difference in the slope between the two groups (control, n= 6 mice; experimental mice, n= 5 mice, *p<0.05).

Figure 6. Loss of the liver-brain axis improves glucose tolerance and insulin sensitivity in male mice.

a. Graph showing that the basal glucose levels were significantly lower in the experimental groups than in the control group (control, n=11 mice; experimental, n=8 mice; unpaired *t*-test, **p<0.01).

b. Graph showing the fasting glucose levels in the control and experimental groups (control, n= 9 mice; experimental, n= 6 mice; unpaired *t*-test, ***p<0.001).

c and **d**. Summary graphs showing the GTT in $Avil^{CreERT2}$ mice with (n= 7 mice) and without (n= 5 mice) liver-projecting vagal sensory neurons (Two-way ANOVA followed by Sidak multiple comparison test, *p<0.05). AUC (**d**) of the control (n= 6 mice) and experimental (n = 5 mice; unpaired t-test, *p < 0.05) groups.

e. Plot showing the ITT in the experimental and control groups (control, n= 10 mice; experimental, n= 9 mice; two-way ANOVA followed by Sidak multiple comparisons test, *p<0.05).

f and **g**. Graphs showing plasma basal and fasting insulin levels in the control (n= 9 and 5 mice, respectively) and experimental groups (n= 10 and 5 mice, respectively, unpaired *t*-test, ***p<0.001, **p<0.01).

Figure 7. Loss of the liver-brain axis improves glucose tolerance in females.

a and **b.** Graphs showing basal (n= 9 vs. 13 mice) and fasting (n=7 vs. 13 mice) glucose levels in the control and experimental groups (unpaired *t*-test, **p<0.01, ***p<0.001).

c and **d**. Summary graphs showing the GTT in Avil^{CreERT2} female mice with (n= 8 mice) and without (n= 11 mice) liver-projecting vagal sensory neurons (two-way ANOVA followed by Sidak multiple comparison test, ***p<0.001). AUC (**d**, unpaired *t*-test, ***p<0.001).

e. Graph showing no difference in the ITT in Avil^{CreERT2} mice with and without liver-projecting vagal sensory neurons (control, n= 10 mice; experimental group, n= 14 mice).

f and **g**. Graphs showing basal plasma and fasting insulin levels in the control (n= 6 mice) and experimental groups (n= 6 mice, unpaired *t*-test, *p<0.05)

Figure 8. Loss of the liver-brain axis prevents hepatic steatosis in male mice.

a. Representative images of liver tissues from the control and experimental mice.

b. Graphs showing liver mass between the groups (n= 14 vs. 18 mice, unpaired *t*-test, **p<0.01)

c. H&E staining of liver tissues showing increased numbers of lipid droplets in control mice compared to those in experimental mice (top panel). Scale bar, 100 μm. Bottom panel: higher-magnification view of the liver tissue in the black dotted square. Scale bar, 30 μm

d. Oil Red O staining of liver tissues from Avil^{CreERT2} mice with and without vagal sensory neurons. The control group showed dense fat accumulation in the liver parenchyma during high -fat diet feeding. Nuclear staining with hematoxylin (blue). Scale bar, 100 μm. Bottom panel: higher-magnification view of the liver tissue in the black dotted square. Scale bar, 30 μm

e. Graph showing hepatic TG levels in the control (n= 7 mice) and experimental groups (n= 7 mice, unpaired *t*-test, ***p<0.001).

f. Summary graphs showing changes in hepatic mRNA expression of enzymes involved in lipid

metabolism between the groups (control, n= 7; experimental, n= 7, unpaired t-test, *p<0.05, **p<0.01, ***p<0.001).

g. Summary graphs showing changes in hepatic mRNA expression of fatty acid uptake transport proteins between the groups (control, n= 6-8 mice; experimental, n= 7 mice, unpaired t-test, *p<0.05, **p<0.01).

Figure 9. Loss of the liver-brain axis prevents hepatic steatosis in female mice.

a. Representative images of liver tissues from the control and experimental mice.

b. Graphs showing that the liver mass of the experimental mice (n=9) was lower when compared to that of the control group (n= 11 mice, unpaired *t*-test, *p<0.05).

c and d. H&E (c) and Oil Red O (d) staining of liver tissues from the control and experimental mice (top panel). Scale bar, 50 μm. Bottom panel: higher-magnification view of the liver tissue. Scale bar, 30 μm. The experimental group showed relatively less fat accumulation in the liver parenchyma (d). Scale bar, 50 μm

e. Graph showing hepatic TG levels in the control (n= 6 mice) and experimental groups (n= 7 mice, unpaired *t*-test, *p<0.05).

f. Summary graph showing alterations in hepatic lipogenic gene expression levels (control, n= 7; experimental mice, n= 8).

g. Summary graph showing changes in hepatic fatty acid uptake transport protein expression levels (control, n= 8; experimental mice, n= 8, unpaired t-test, *p<0.05, **p<0.01).

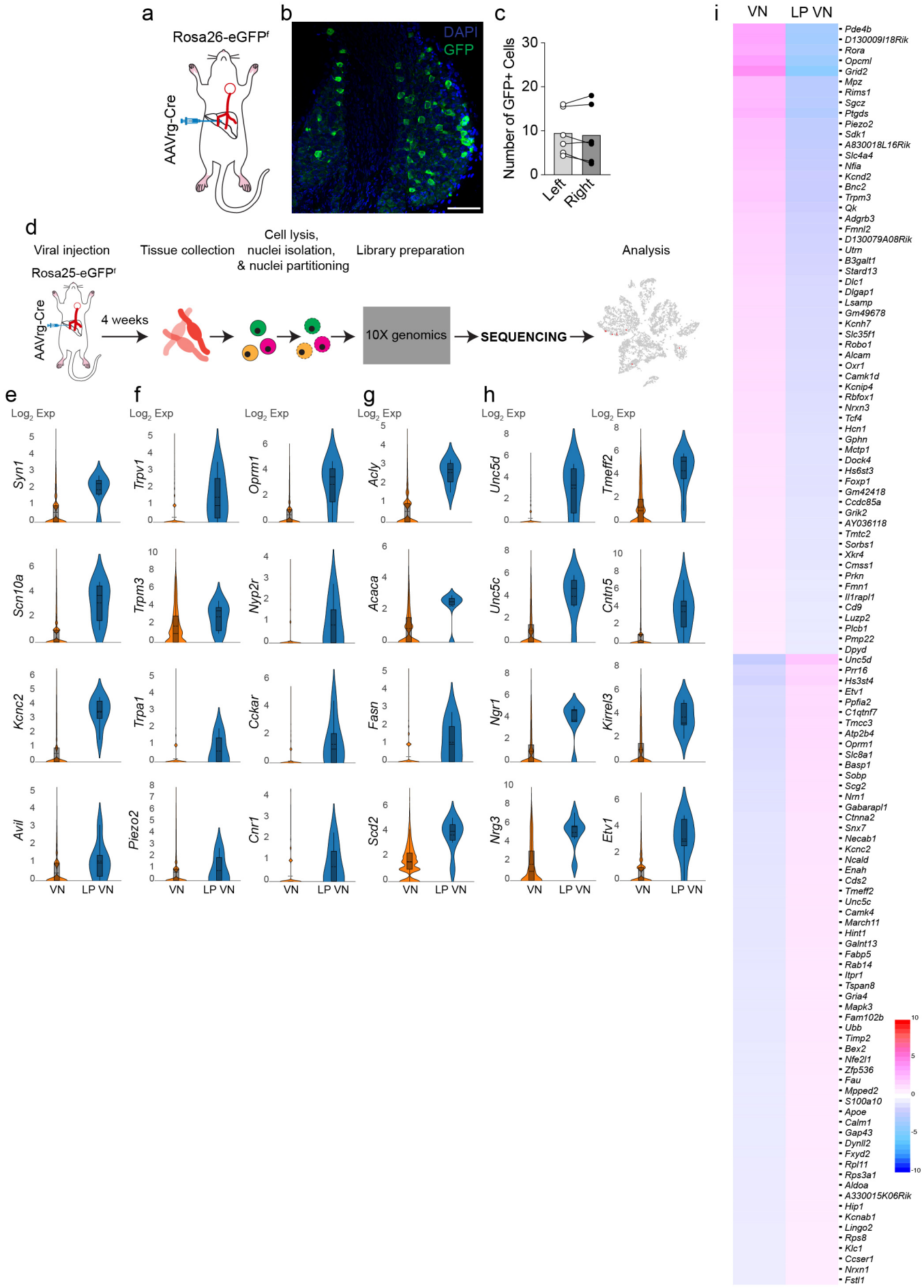
a
Rosa26-eGFP^f
AAVrg-Cre
b
DAPI
GFP
c
Number of GFP+ Cells
Left
Right
d
Viral injection
Rosa25-eGFP^f
AAVrg-Cre
4 weeks
Tissue collection
Cell lysis, nuclei isolation, & nuclei partitioning
Library preparation
10X genomics
SEQUENCING
Analysis
e
f
g
h
Log$_2$ Exp
Syn1
Scn10a
Kcnc2
Avil
Trpv1
Trpm3
Trpa1
Piezo2
Oprm1
Nyp2r
Cckar
Cnr1
Acly
Acaca
Fasn
Scd2
Unc5d
Unc5c
Ngr1
Nrg3
Tmeff2
Cntn5
Kirrel3
Etv1
VN
LP VN
i
VN
LP VN
Pde4b
D130009I18Rik
Rora
Opcml
Grid2
Mpz
Rims1
Sgcz
Ptgds
Piezo2
Sdk1
A830018L16Rik
Slc4a4
Nfia
Kcnd2
Bnc2
Trpm3
Qk
Adgrb3
Fmnl2
D130079A08Rik
Utrn
B3galt1
Stard13
Dlc1
Dlgap1
Lsamp
Gm49678
Kcnh7
Slc35f1
Robo1
Alcam
Oxr1
Camk1d
Kcnip4
Rbfox1
Nrxn3
Tcf4
Hcn1
Gphn
Mctp1
Dock4
Hs6st3
Foxp1
Gm42418
Ccdc85a
Grik2
AY036118
Tmtc2
Sorbs1
Xkr4
Cmss1
Prkn
Fmn1
Il1rapl1
Cd9
Luzp2
Plcb1
Pmp22
Dpyd
Unc5d
Prr16
Hs3st4
Etv1
Ppfia2
C1qtnf7
Tmcc3
Atp2b4
Oprm1
Slc8a1
Basp1
Sobp
Scg2
Nrn1
Gabarapl1
Ctnna2
Snx7
Necab1
Kcnc2
Ncald
Enah
Cds2
Tmeff2
Unc5c
Camk4
March11
Hint1
Galnt13
Fabp5
Rab14
Itpr1
Tspan8
Gria4
Mapk3
Fam102b
Ubb
Timp2
Bex2
Nfe2l1
Zfp536
Fau
Mpped2
S100a10
Apoe
Calm1
Gap43
Dynll2
Fxyd2
Rpl11
Rps3a1
Aldoa
A330015K06Rik
Hip1
Kcnab1
Lingo2
Rps8
Klc1
Ccser1
Nrxn1
Fstl1

Figure 1

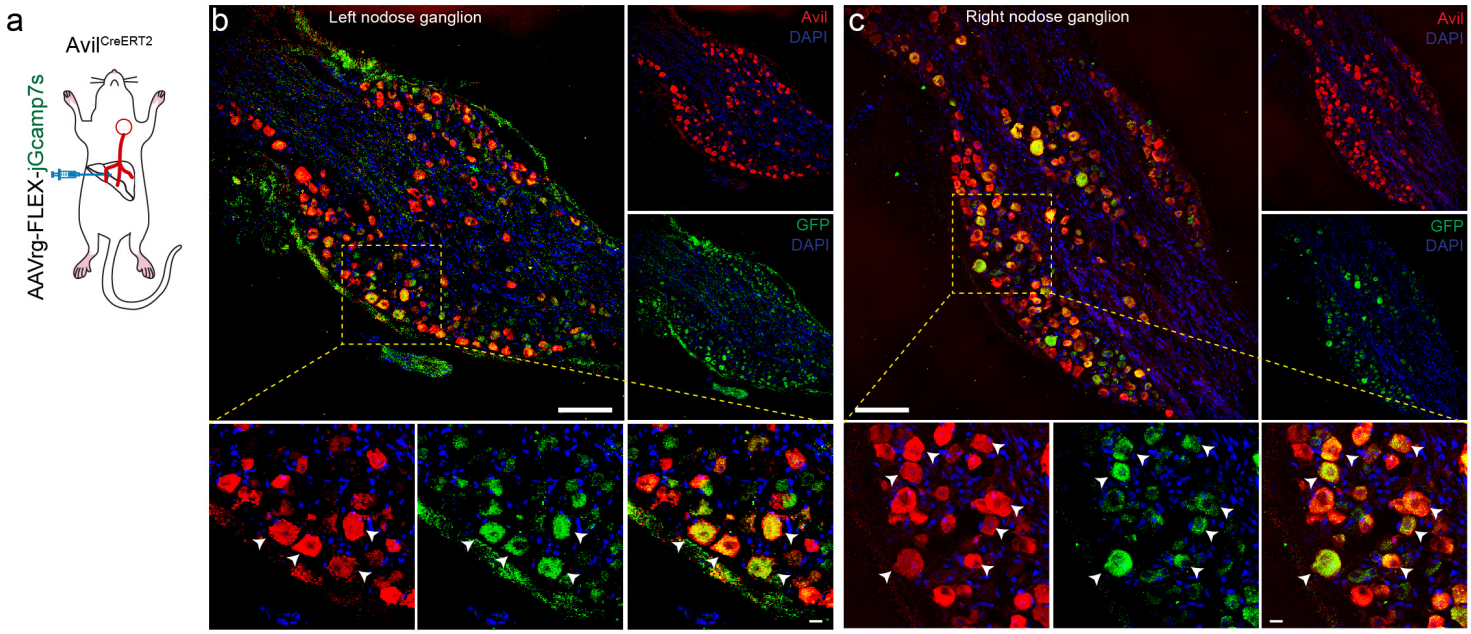
a
AvilCreERT2
AAVrg-FLEX-jGcamp7s
b
Left nodose ganglion
Avil
DAPI
GFP
DAPI
c
Right nodose ganglion
Avil
DAPI
GFP
DAPI

Figure 2

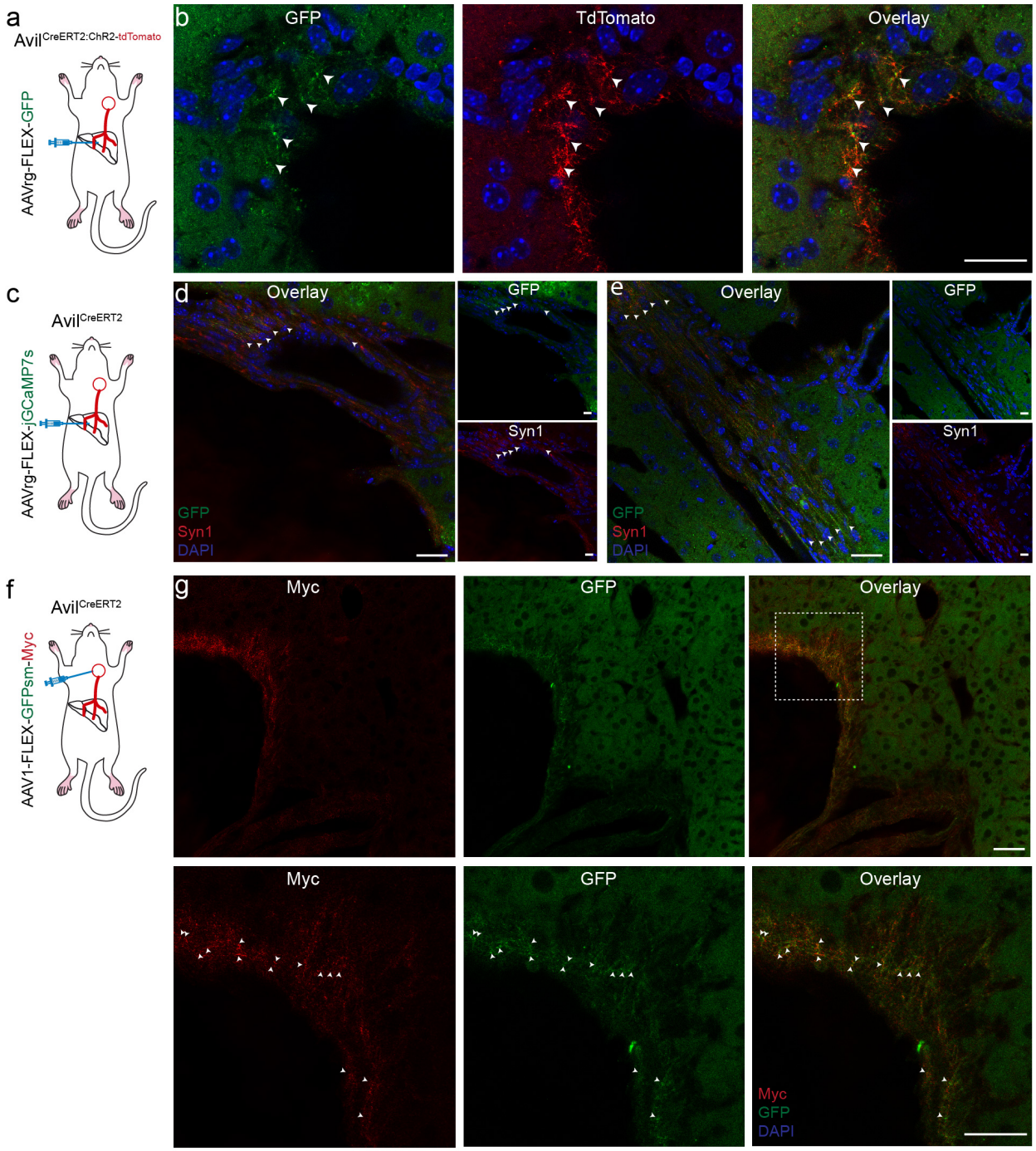
a
AvilCreERT2:ChR2-tdTomato
AAVrg-FLEX-GFP
b
GFP
TdTomato
Overlay
c
AvilCreERT2
AAVrg-FLEX-jGCaMP7s
d
Overlay
GFP
Syn1
GFP
Syn1
DAPI
e
Overlay
GFP
Syn1
GFP
Syn1
DAPI
f
AvilCreERT2
AAV1-FLEX-GFPsm-Myc
g
Myc
GFP
Overlay
Myc
GFP
Overlay
Myc
GFP
DAPI

Figure 3

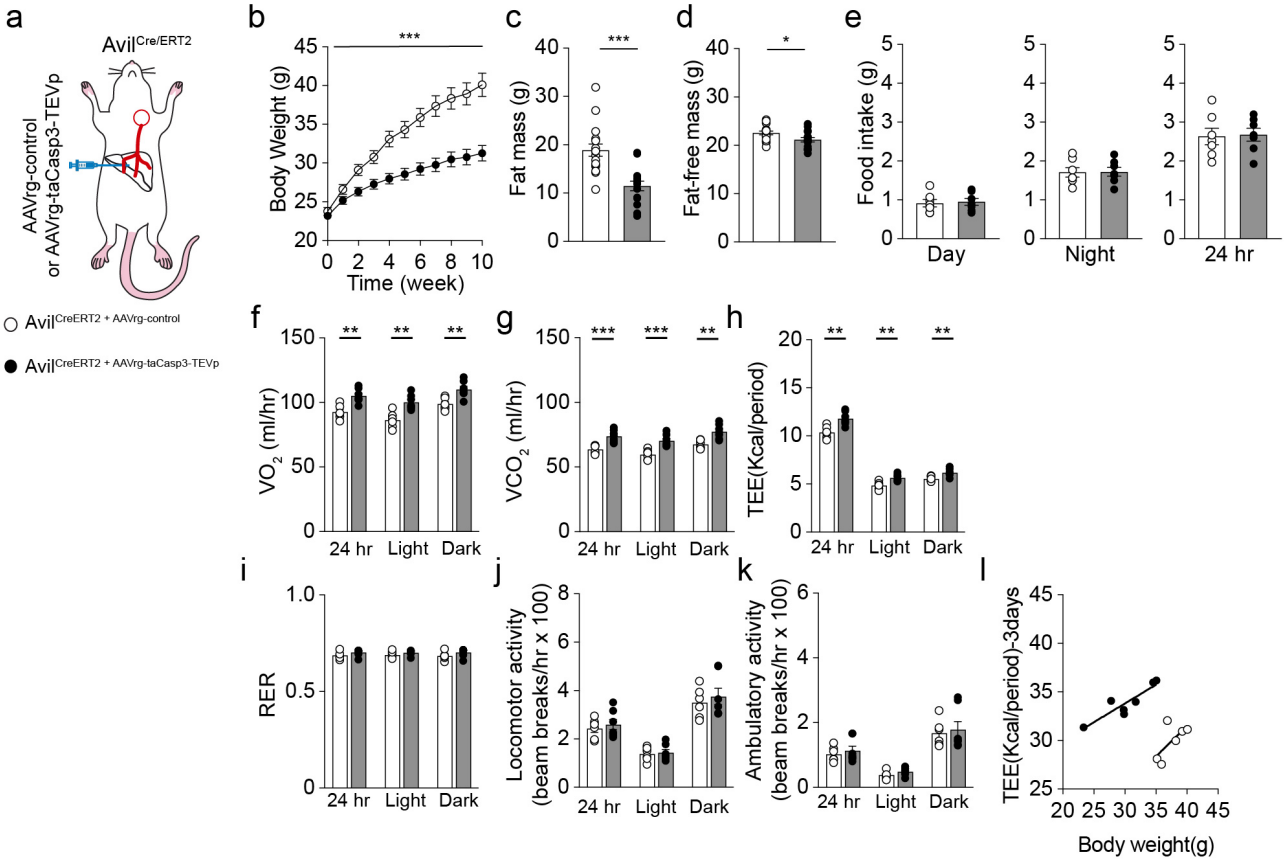
a
AvilCre/ERT2
AAVrg-control
or AAVrg-taCasp3-TEVp
AvilCreERT2 + AAVrg-control
AvilCreERT2 + AAVrg-taCasp3-TEVp
b
Body Weight (g)
Time (week)
c
Fat mass (g)
d
Fat-free mass (g)
e
Food intake (g)
Day
Night
24 hr
f
VO2 (ml/hr)
g
VCO2 (ml/hr)
h
TEE(Kcal/period)
24 hr
Light
Dark
i
RER
j
Locomotor activity
(beam breaks/hr x 100)
k
Ambulatory activity
(beam breaks/hr x 100)
l
TEE(Kcal/period)-3days
Body weight(g)

Figure 4

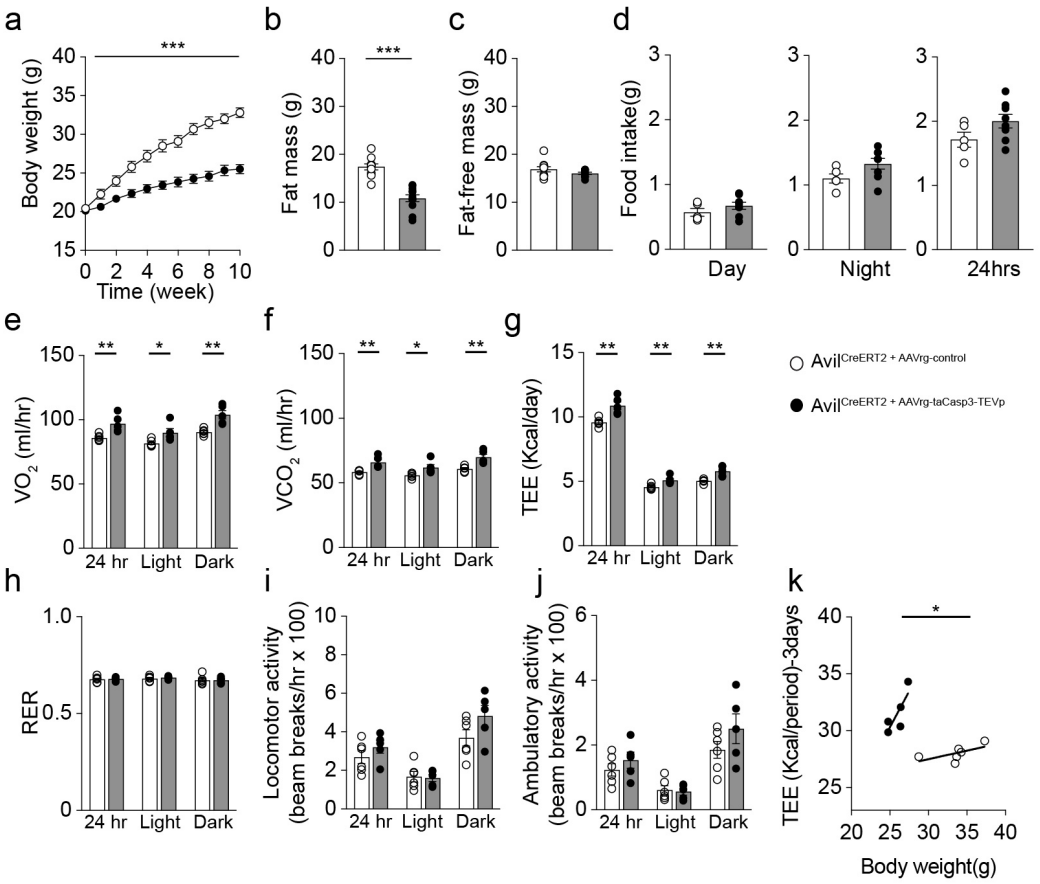
a
b
c
d
Body weight (g)
Time (week)
Fat mass (g)
Fat-free mass (g)
Food intake(g)
Day
Night
24hrs
e
f
g
VO2 (ml/hr)
VCO2 (ml/hr)
TEE (Kcal/day)
24 hr
Light
Dark
AvilCreERT2 + AAVrg-control
AvilCreERT2 + AAVrg-taCasp3-TEVp
h
i
j
k
RER
Locomotor activity (beam breaks/hr x 100)
Ambulatory activity (beam breaks/hr x 100)
TEE (Kcal/period)-3days
Body weight(g)

Figure 5

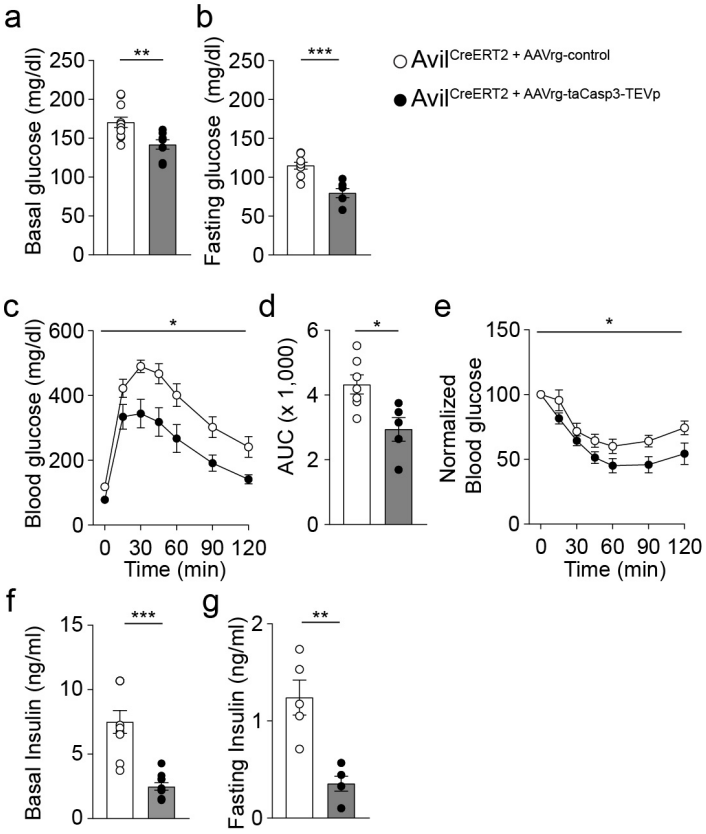
a
b
Basal glucose (mg/dl)
Fasting glucose (mg/dl)
**
***
AvilCreERT2 + AAVrg-control
AvilCreERT2 + AAVrg-taCasp3-TEVp
c
d
e
Blood glucose (mg/dl)
AUC (x 1,000)
Normalized Blood glucose
Time (min)
*
f
g
Basal Insulin (ng/ml)
Fasting Insulin (ng/ml)

Figure 6

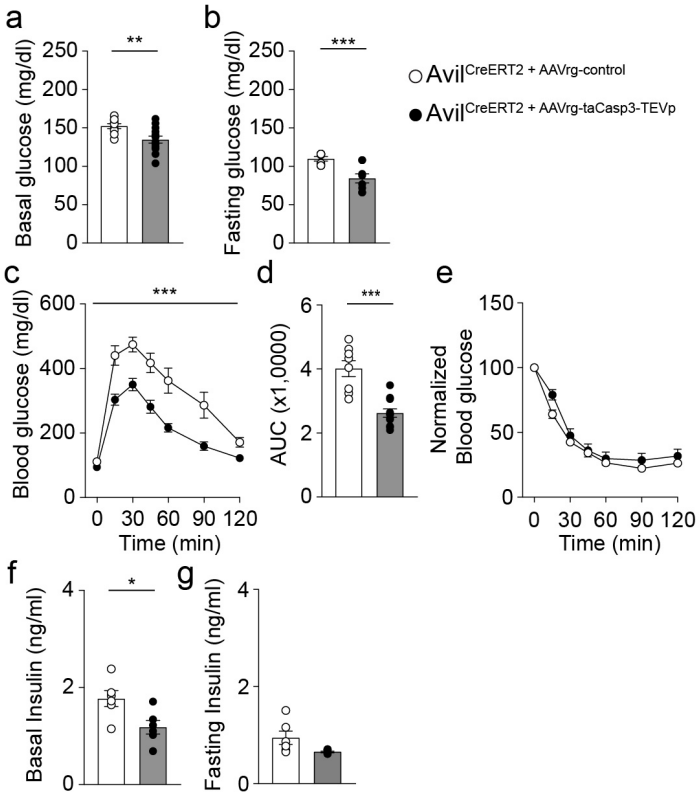
a
b
c
d
e
f
g
Basal glucose (mg/dl)
Fasting glucose (mg/dl)
Blood glucose (mg/dl)
AUC (x1,0000)
Normalized Blood glucose
Basal Insulin (ng/ml)
Fasting Insulin (ng/ml)
Time (min)
Avil CreERT2 + AAVrg-control
Avil CreERT2 + AAVrg-taCasp3-TEVp

Figure 7

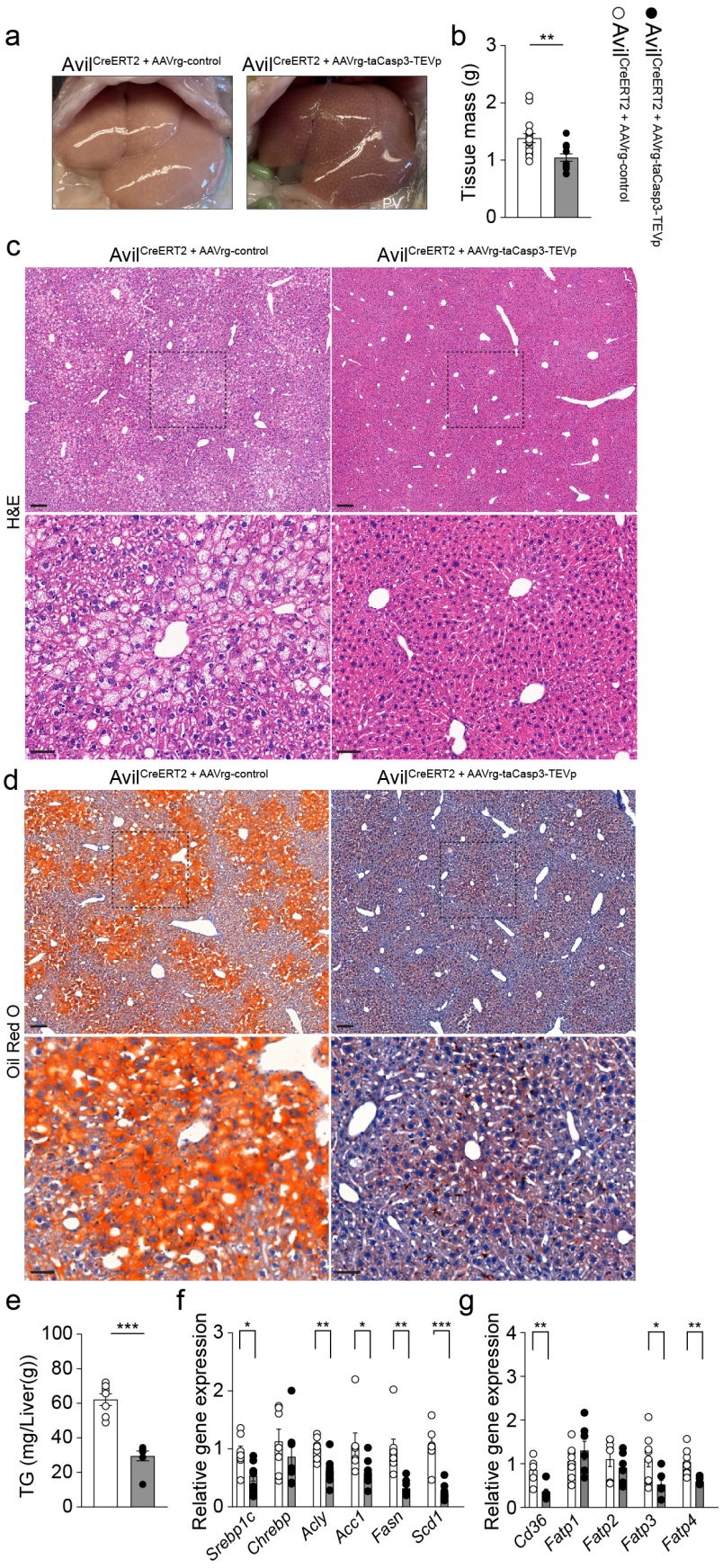
a
AvilCreERT2 + AAVrg-control
AvilCreERT2 + AAVrg-taCasp3-TEVp
PV
b
Tissue mass (g)
**
AvilCreERT2 + AAVrg-control
AvilCreERT2 + AAVrg-taCasp3-TEVp
c
H&E
d
Oil Red O
e
TG (mg/Liver(g))
***
f
Relative gene expression
Srebp1c
Chrebp
Acly
Acc1
Fasn
Scd1
g
Cd36
Fatp1
Fatp2
Fatp3
Fatp4

Figure 8

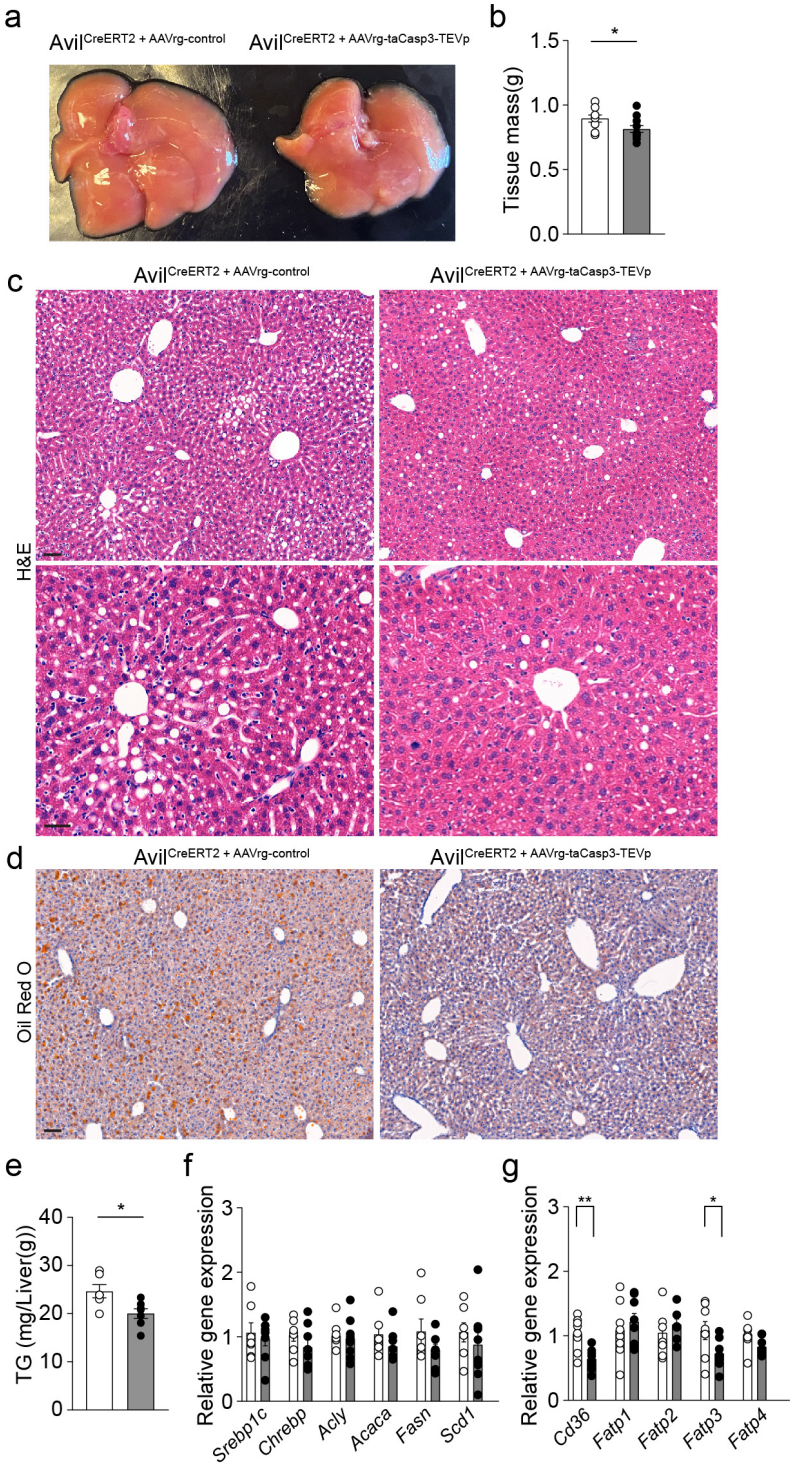
a
AvilCreERT2 + AAVrg-control
AvilCreERT2 + AAVrg-taCasp3-TEVp
b
Tissue mass(g)
1.5
1.0
0.5
0.0
*
c
AvilCreERT2 + AAVrg-control
AvilCreERT2 + AAVrg-taCasp3-TEVp
H&E
d
AvilCreERT2 + AAVrg-control
AvilCreERT2 + AAVrg-taCasp3-TEVp
Oil Red O
e
TG (mg/Liver(g))
40
30
20
10
0
*
f
Relative gene expression
3
2
1
0
Srebp1c
Chrebp
Acly
Acaca
Fasn
Scd1
g
Relative gene expression
3
2
1
0
**
*
Cd36
Fatp1
Fatp2
Fatp3
Fatp4

Figure 9

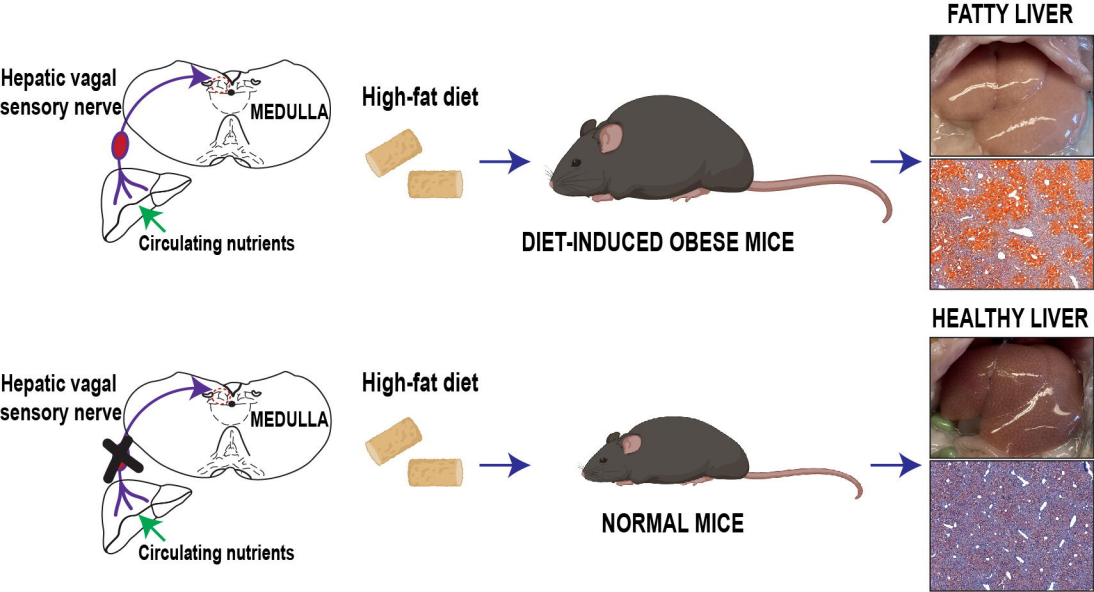
FATTY LIVER
Hepatic vagal sensory nerve
MEDULLA
High-fat diet
Circulating nutrients
DIET-INDUCED OBESE MICE
HEALTHY LIVER
Hepatic vagal sensory nerve
MEDULLA
High-fat diet
Circulating nutrients
NORMAL MICE